Geophysical Research Letters

RESEARCH LETTER
10.1029/2024GL113368

Propagation of EMIC Waves From Shabansky Orbits in the Dayside Magnetosphere

Eun-Hwa Kim[1,2], Syun'ichi Shiraiwa[1], Jay R. Johnson[3], Nicola Bertelli[1], Sarah K. Vines[4], Khan-Hyuk Kim[5], Mark Engebretson[6], Hyomin Kim[7], and Carson O'ffill[3]

[1]Princeton Plasma Physics Laboratory, Princeton University, Princeton, NJ, USA, [2]Department of Physics, Andrews University, Berrien Springs, MI, USA, [3]School of Engineering, Andrews University, Berrien Springs, MI, USA, [4]Southwest Research Institute, San Antonio, TX, USA, [5]School of Space Research, Kyung Hee University, Yongin, South Korea, [6]Department of Physics, Augsburg University, Minneapolis, MN, USA, [7]New Jersey Institute of Technology, Newark, NJ, USA

Key Points:

- EMIC waves are examined in a compressed magnetic field in the outer dayside magnetosphere
- The Poynting vector of EMIC waves consistently changes based on the local source location of the wave
- EMIC wave power in the outer magnetosphere can show significant interhemispheric asymmetry

Correspondence to:
E.-H. Kim,
ehkim@pppl.gov

Citation:
Kim, E.-H., Shiraiwa, S., Johnson, J. R., Bertelli, N., Vines, S. K., Kim, K.-H., et al. (2025). Propagation of EMIC waves from Shabansky orbits in the dayside magnetosphere. *Geophysical Research Letters*, *52*, e2024GL113368. https://doi.org/10.1029/2024GL113368

Received 3 NOV 2024
Accepted 22 JAN 2025

Author Contributions:
Conceptualization: Eun-Hwa Kim, Jay R. Johnson, Khan-Hyuk Kim
Formal analysis: Eun-Hwa Kim, Sarah K. Vines, Carson O'ffill
Funding acquisition: Eun-Hwa Kim, Nicola Bertelli
Investigation: Eun-Hwa Kim, Jay R. Johnson, Sarah K. Vines
Methodology: Eun-Hwa Kim, Syun'ichi Shiraiwa, Nicola Bertelli
Project administration: Eun-Hwa Kim
Software: Syun'ichi Shiraiwa, Nicola Bertelli
Supervision: Eun-Hwa Kim
Validation: Syun'ichi Shiraiwa
Visualization: Eun-Hwa Kim, Sarah K. Vines
Writing – original draft: Eun-Hwa Kim, Sarah K. Vines
Writing – review & editing: Jay R. Johnson, Sarah K. Vines, Khan-Hyuk Kim, Mark Engebretson, Hyomin Kim

Abstract We explore the characteristics of EMIC waves generated in a non-dipole, compressed magnetic field at the minimum of the magnetic field. We conducted 2D full-wave simulations using the Petra-M code, focusing on a compressed magnetic field in the outer dayside magnetosphere for a range of L values ($L = 8 - 10$). By comparing the simulation results with MMS observations, we aim to understand how the observed wave characteristics are affected by a shifting source region across different L-shells. Our findings indicate that the direction of the Poynting vector systematically changes depending on the local source location of the wave, which is consistent with the observations. EMIC waves propagate along the magnetic field line and reach both the northern and southern hemispheres; however, there is a notable difference in the power of EMIC waves between the two hemispheres, indicating seasonal asymmetries in their occurrence.

Plain Language Summary Electromagnetic ion cyclotron (EMIC) waves, with frequencies ranging from 0.1 to 5 Hz, are commonly found in Earth's magnetosphere. These waves can be detected in the outer dayside magnetosphere, where the interaction between Earth's magnetic field and the solar wind causes the magnetic field lines to compress. EMIC waves can be generated at points where the magnetic field strength becomes minimum in each magnetic field line, meaning the magnetic latitude of the source location can vary for each L-shell. We conducted a full-wave simulation of EMIC waves in the outer dayside magnetosphere using the Petra-M code, incorporating a non-dipole compressed magnetic field. Our results indicated that the direction of wave energy flow from the source varies; thus, based on a satellite's location, it can detect wave energy flowing either parallel or antiparallel to the magnetic field, which is consistent with satellite observations. We also show that EMIC waves generated in the northern hemisphere can reach both the north and the south Polar Regions. However, the wave power reaching the northern hemisphere is significantly stronger than that which reaches the southern hemisphere.

1. Introduction

Known for decades, electromagnetic ion cyclotron (EMIC) waves in the Pc 1–2 (0.1–5 Hz) frequency range have been observed to be a prominent feature of the Earth magnetosphere-ionosphere system (e.g., Bashir & Ilie, 2021; Blum et al., 2020; Chen et al., 2019; Engebretson et al., 2018; Jun et al., 2021; G.-J. Kim et al., 2016; K.-H. Kim et al., 2017; Noh et al., 2022; Saikin et al., 2015; Toledo-Redondo et al., 2024; Usanova et al., 2016) and other magnetized planets (e.g., Yao et al., 2021; Yuan et al., 2024). These waves are known to be excited as left-handed polarized (LHP) waves by the ion cyclotron instability of hot and anisotropic $\left(T_{\perp} > T_{\parallel}\right)$ distributions (Anderson et al., 1996; Cornwall, 1965; Jordanova et al., 2001; Kozyra et al., 1997; Taylor & Lyons, 1976; Thorne et al., 2006) or as linearly polarized waves by mode-conversion at the ion-ion hybrid resonance (E.-H. Kim et al., 2015; E.-H. Kim & Johnson, 2023; Klimushkin et al., 2010; D.-H. Lee et al., 2008; Mikhailova et al., 2019; Xu & Zhou, 2023; Xu et al., 2023). EMIC waves play an important role in the exchange of particle energy in the magnetosphere. These waves interact with energetic ring current ions and radiation belt electrons (Albert & Bortnik, 2009; Shprits et al., 2016; Summers & Thorne, 2003; Usanova, 2021; Usanova et al., 2014; Yu et al., 2019). EMIC waves can also interact with cold ions with energies of a few electron volts or less (M. J. Kim, Goldstein, et al., 2023; K.-H. Kim, Jun, et al., 2024; Kwon et al., 2023; J. Lee, Kim, & Lee, 2021; Mauk, 1982; Mouikis et al., 2002; Roux et al., 1982).

EMIC waves are frequently observed across a wide range of L-shells in the outer dayside magnetosphere (Allen et al., 2015, 2016; Min et al., 2012; Noh et al., 2023; Vines et al., 2019; Wang et al., 2017). Particles in the compressed magnetosphere region undergo peculiar Shabansky orbits that enhance anisotropy in the high-latitude region by breaking the second adiabatic invariant (Shabansky, 1971). Additionally, the minimum of the magnetic field along a field line moves to higher latitude in both hemispheres as L-shell increases for a compressed magnetic field configuration (McCollough et al., 2010, 2012). Thus, the region of EMIC wave generation is similarly expected to change in latitude. Such off-equator source regions at high latitudes in the dayside magnetosphere were suggested to be present in case studies and statistical observations from the Cluster mission (Allen et al., 2013, 2016). Observations from the Magnetospheric Multiscale (MMS) mission detected a shift in the direction of the Poynting flux concurrent with plasma conditions favorable to local generation as the satellites passed from the outer to the inner magnetosphere, indicating that MMS flew through a source region at high latitudes in the outer magnetosphere (Vines et al., 2019).

The EMIC waves generated in the outer magnetosphere can reach the ground near the polar region. The occurrence of EMIC waves at the Antarctic station exhibited seasonal asymmetry (Regi et al., 2017), with a higher occurrence in local summer than in local winter. The hemispheric asymmetry in the arrival time of EMIC waves can also occur in the outer magnetosphere (Noh et al., 2023). The observed time differences between the hemispheres suggested that the source region of the wave was in an off-equatorial region.

Since satellite observations alone are insufficient for capturing the global characteristics of wave propagation, numerical simulations are essential for understanding the global features of EMIC wave propagation along the Earth's magnetic field lines. Previous simulations have been conducted in the Earth's magnetosphere using the dipole magnetic field model (Denton, 2018; Hanzelka et al., 2023; Hu & Denton, 2009; E.-H. Kim & Johnson, 2016, 2023; Omidi et al., 2011; Pakhotin et al., 2022). However, to better understand the propagation of EMIC waves in the dayside outer magnetosphere, it is crucial to utilize non-dipole compressed magnetic field models (Cheng, 1995; Stern, 1967) integrated into the existing wave model (E.-H. Kim, Shiraiwa, et al., 2023).

In this letter, we numerically investigate the characteristics of EMIC waves generated off-equator related to regions of Shabansky orbits, employing a non-dipole magnetic field configuration in the dayside magnetosphere. We perform full-wave simulations covering the outer magnetosphere within the range $8 \leq L \leq 10$ and analyze the wave electric field strength, ellipticity, and Poynting fluxes. In addition, we explore the wave properties as they propagate to the ionosphere from the source.

The structure of this paper is as follows: Section 2 provides an overview of the Petra-M full-wave simulation code and displays the simulation results. We first present wave solutions across different L-shells, followed by the characteristics of EMIC waves observed by virtual satellites on various paths. In the last section, we compare these simulated wave properties with observations and discuss the EMIC wave propagation.

2. Full-Wave Simulations

We adopt the Petra-M full-wave simulation code. Petra-M is an open-source finite element method platform based on a scalable MFEM finite element library (Shiraiwa et al., 2016, 2017). In this platform, the cold plasma wave equation has been solved,

$$\nabla \times \left(\nabla \times \mathbf{E}/\mu_0\right) - \underline{\epsilon}\omega^2\mathbf{E} - i\omega\mathbf{J}_{in} = i\omega\mathbf{J}_{ext}, \tag{1}$$

where $\mathbf{E}$ is the perturbed electric field, $\mathbf{J}_{in} = \underline{\sigma} \cdot \mathbf{E}$ is the perturbed current density, $\mathbf{J}_{ext}$ is the external current source that generates waves within our model, $\underline{\epsilon}$ is the permittivity tensor, μ_0 is the permeability of free space, and $\underline{\sigma}$ is the conductivity tensor. This code has been widely used for plasma wave simulations in fusion devices (Bertelli et al., 2022, 2023; E.-H. Kim, Ono, et al., 2024; Shiraiwa, Bertelli, Tierens, et al., 2023; Shiraiwa, Bertelli, Bilato, et al., 2023), in Earth's magnetosphere (E.-H. Kim & Johnson, 2023; E.-H. Kim, Shiraiwa, et al., 2023), and also adopted for high-temperature conductors (Mohebujjaman et al., 2023).

For 2D simulations in cylindrical coordinates, we use the simulation domain $0.1 < r/\mathrm{R_E} < 11.5$ and $-11 < z/\mathrm{R_E} < 11$ (or $-3 < z/\mathrm{R_E} < 11$ when we focus on the northern hemisphere) to encompass the outer magnetosphere, with R_E representing the Earth's radius. Similarly to previous works (E.-H. Kim & Johnson, 2016, 2023; E.-H. Kim, Shiraiwa, et al., 2023), a collisional absorption layer near the boundary is included for an open

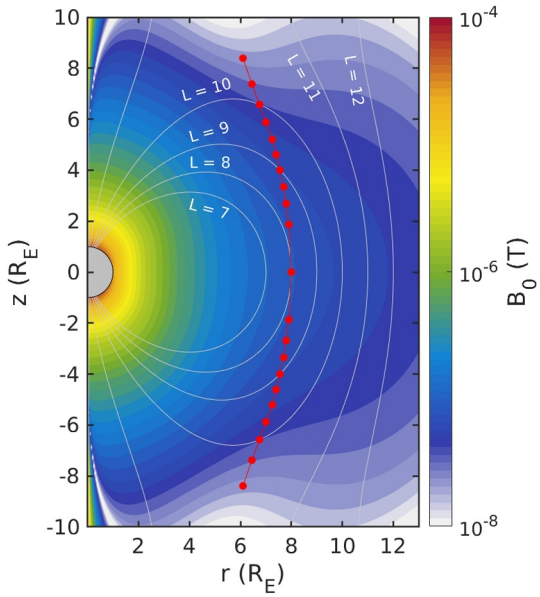

Figure 1. Simulation parameters: The magnetic field strength (B_0) and magnetic flux line (white solid lines). Here, the red points represent the location where the magnetic field is minimized in each L-shell.

space. This layer efficiently absorbs all waves, allowing them to exit the simulation domain without reflection. The Earth is assumed to be a perfect conductor; however, strong absorption is also applied at $R = 2$ R_E as a Gaussian function, where $R = \sqrt{r^2 + z^2}$ is the geocentric distance, to minimize wave reflection from the Earth's surface.

To analyze the dayside magnetic field configuration, we integrate the magnetic field model developed by Stern (1967) (hereafter referred to as Stern's model) into the Petra-M code. We determine the unit vector of the magnetic field in cylindrical coordinates ($\hat{b}_r$, $\hat{b}_\phi$, $\hat{b}_z$) along with the magnitude of the background magnetic field (B_0). Figure 1 shows the non-dipole magnetic field lines and B_0 as derived from Stern's model. In this figure, the red dots mark the locations of the minimum B_0 within each L-shell. At $L = 8$, the magnetic field exhibits a weak compression, yet the minimum B_0 remains at the magnetic equator. As the L-shell increases, the magnetic latitude (λ_{B0}) corresponding to the minimum B_0 also rises from $\lambda_{B0} = 0°$, 28°, and 44° for $L = 8$, 9, and 10, respectively.

We employ an empirical electron density model from Denton et al. (2006), defined by

$$N_e = 1390\left(\frac{3}{L}\right)^{4.83}\left(\frac{L}{R/R_E}\right)^{0.8}, \quad (2)$$

where L represents a modified L-shell as depicted in Figure 1. In this paper, we do not consider realistic ionospheric density and conductivity. We also exclude heavy-ion effects to focus on the influence of the magnetic field configuration.

We launch left-hand polarized waves with $f = 0.34$ Hz at the northern hemisphere source locations, which are indicated by red dots in Figure 1. These dots are the location of minimum B along the field line where wave growth is maximum due to higher temperature anisotropy and increased plasma beta (McCollough et al., 2010, 2012). This choice of frequency is motivated by observations of EMIC waves from Vines et al. (2019). At the source locations with $L = 8 - 10$, the ratio of wave frequency (ω) to the local ion cyclotron frequency (ω_{ci}) is $\omega/\omega_{ci} = 0.22 - 0.5$. ω at $L = 8$ is lower than the He^+ cyclotron frequency; however, these waves can be treated as H-band EMIC waves in a single-ion plasma. We assume that the wavefront is perpendicular to the field line at the center of the source and that the source's cross-field dimension is larger than the dimension along the field line, channeling the waves to propagate along the magnetic field. For simplicity, the azimuthal wavenumber is assumed to be 0. For the given condition, the field-aligned wavelength for each field line is $0.246 - 0.152$ R_E, respectively. In order to describe the wavelength of the EMIC waves near the outer magnetosphere and to consider magnetic field line separation near the Earth, non-uniform triangle meshes are adopted.

2.1. Wave Propagation in the Compressed Magnetic Field Line

Figure 2 shows the propagation of EMIC waves initiated in various L-shells. The columns displayed from the left to the right in Figure 2 are the electric field components perpendicular to the magnetic field in the meridian plane (E_η), in the azimuthal direction (E_ϕ), the field-aligned Poynting flux ($S_\parallel$), and the ellipticity (ϵ), respectively. The electric field and the Poynting flux are normalized with respect to the maximum values of the total electric field strength (E_{max}) or the total Poynting flux strength (S_{max}).

For the case of $L = 8$, as shown in Figure 2a–2d, the wave source is located at the magnetic equator. The waves propagate along the field line toward Earth. As the waves move to higher magnetic latitudes, the wave polarization rapidly changes from left-handed (LHP) to linear in E_η (see Figures 2a and 2d). Since strong artificial absorption near Earth is adopted, no wave power is detected below the ionospheric altitude. Given that the shape of the magnetic field line and the source location exhibit symmetry between the northern and southern hemispheres, $S_\parallel$ also exhibits interhemispheric symmetry except for the sign.

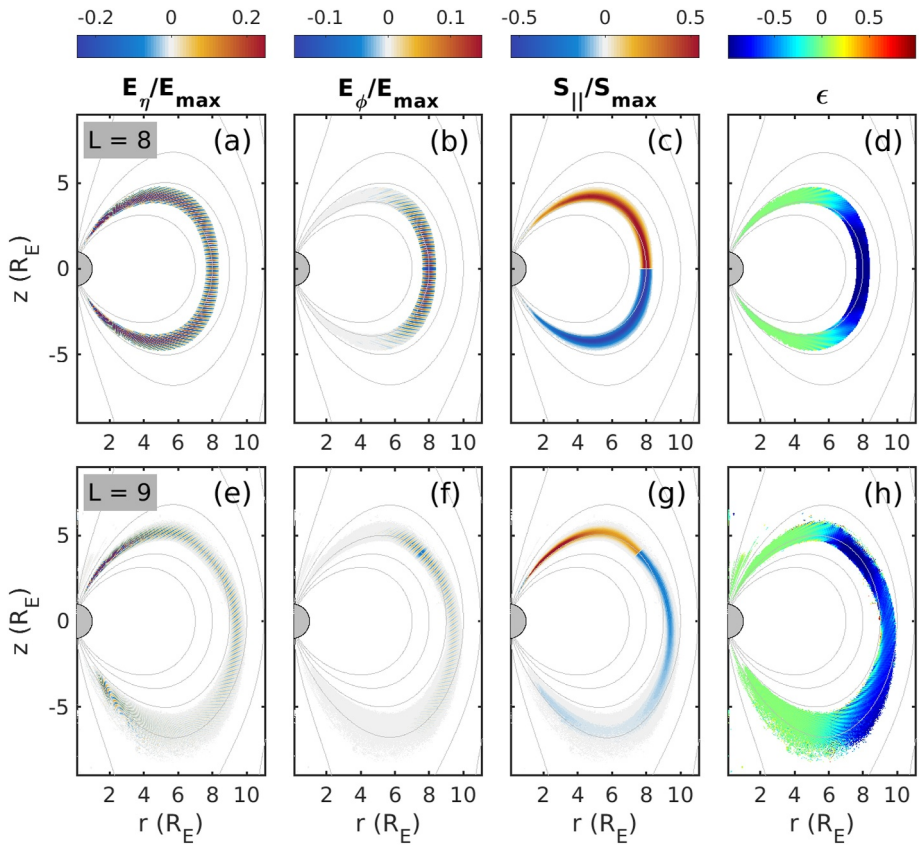

Figure 2. Wave solutions at (a–d) $L = 8$ and (e–h) $L = 9$, respectively. From left to right, the electric field in the direction perpendicular to the magnetic field in the meridian plane (E_η), in the azimuthal direction (E_ϕ), the field-aligned Poynting flux $(S_\parallel)$, and the ellipticity (ϵ), respectively. The electric field and the Poynting flux are normalized with respect to the maximum values of the total electric field strength $(E_{\max})$ or the total Poynting flux strength $(S_{\max})$. For Poynting flux, positive and negative values are parallel and antiparallel directions, and for the ellipticity, +1 (red color), −1 (blue), and 0 (green) indicate circularly right-handed, left-handed, and linear polarization, respectively.

When the waves are launched at higher magnetic latitude $(L = 9)$ in Figures 2e and 2f, an asymmetric structure of the EMIC wave power distribution is found between the northern and southern hemispheres, although the plasma configuration is the same for both hemispheres. When the waves propagate toward the north pole, the LHP waves rapidly transform into linearly polarized waves and propagate to ionospheric altitudes, as shown in Figures 2e and 2h. Despite our implementation of strong absorption near the ionosphere, the wave power still reaches near the ionosphere. Left-handed polarized waves propagating southward from the source are effectively guided by $\mathbf{B}_0$. This wave mode propagates roughly parallel to the magnetic field line and extends slightly to larger L-shells. As a result, it spans a wide range of L-shells during its propagation, and the center of the ray path reaches near $L = 10$ at the southernmost point of the field line. As shown in Figure 2, the waves can spread over a wider range of L-shells, which leads to significantly weaker wave power per L-shell compared to the northern hemisphere. As circular LHP waves propagate toward lower latitudes, they transition to elliptical polarization; the ellipticity changes from −1 at the source and near the magnetic equator to approximately −0.33. Ultimately, waves become linearly polarized near the southernmost point. The field-aligned Poynting flux is positive, parallel to $\mathbf{B}_0$, when the magnetic latitude is higher than the source location. For magnetic latitudes below the source location, it is negative and antiparallel to $\mathbf{B}_0$.

2.2. EMIC Waves Detected by Virtual Satellites

By assuming that the waves are simultaneously generated via Shabansky orbits at local minima in the magnetic field across various L-shells, we evaluate the wave polarization and field-aligned Poynting flux along trajectories of virtual spacecraft. To account for simultaneous wave generation over different locations, we superpose the

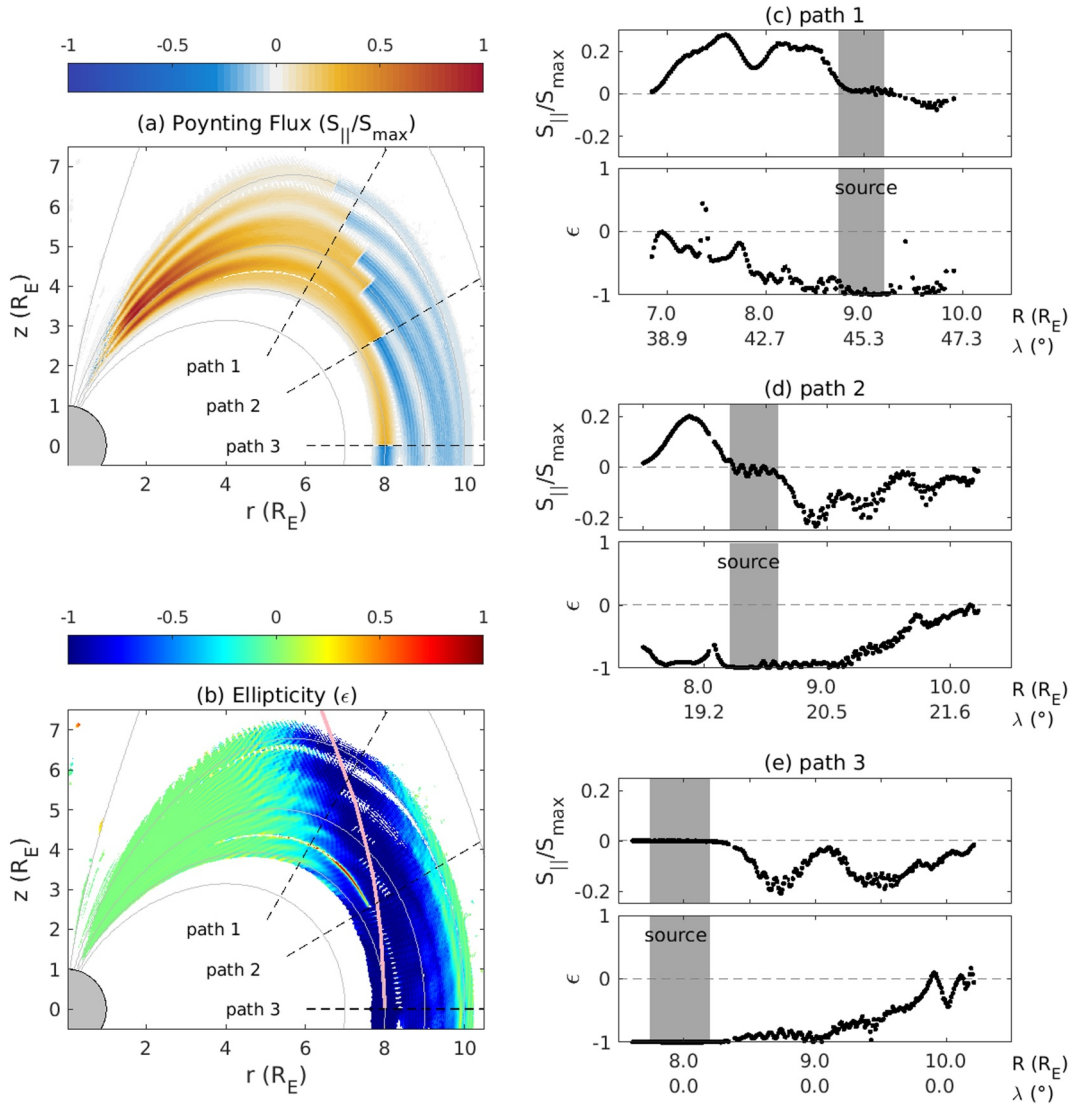

Figure 3. Superposition of the wave solutions at $L = 8$, 8.5, 9.0, 9.3, 9.7, and 10; (a) Normalized field-aligned Poynting flux and (b) Ellipticity (ϵ). Here, the dashed lines are traces of the virtual spacecraft, and the solid pink line indicates the Shabansky orbit (c)–(e) Measured Poynting flux and ellipticity of EMIC waves generated at three virtual spacecraft. The gray shades in (c)–(e) are the source locations of $L = 9.7$, 8.5, and 8, respectively. Here, $R = \sqrt{r^2 + z^2}$ is the geocentric distance, and λ is the magnetic latitude.

wave solutions of the electric and magnetic fields at $L = 8$, 8.5, 9.0, 9.3, 9.7, and 10, respectively. In this case, we conduct simulations in the northern hemisphere to focus wave polarization and Poynting flux variations from the source to the ground. The total electric field ($\mathbf{E}_{tot}$) and the magnetic field ($\mathbf{B}_{tot}$) are the sum of the individual electromagnetic fields. We then compute the Poynting flux and the ellipticity of the resulting electromagnetic field using $\mathbf{E}_{tot}$ and $\mathbf{B}_{tot}$.

Figure 3a shows that the field-aligned Poynting flux is bidirectional near the source location, indicating that waves propagate outward from the source. It becomes positive or negative at latitudes higher or lower than the source location. Left-hand polarization is found near the source, as shown in Figure 3b. The northward-propagating waves quickly transition to linear polarization across all L-shells. However, the southward propagating waves in the inner L-shells still appear as LHP near the magnetic equator. In contrast, the waves in the outermost L-shells become linearly polarized as soon as they escape from the source location. Consequently, the

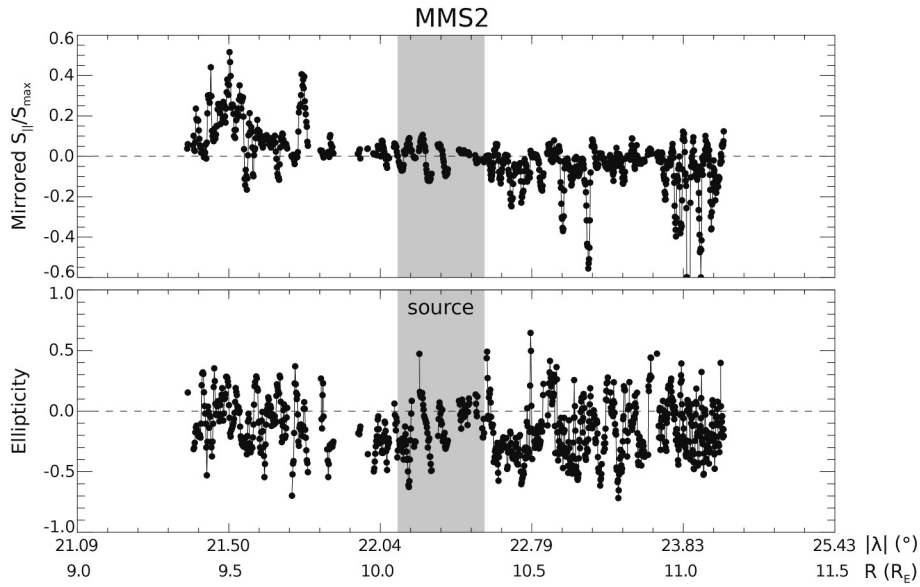

Figure 4. MMS2 EMIC wave observations from 2015-10-28/14:30 - 17:15 UT, showing (a) normalized field-aligned Poynting flux mirrored to the northern hemisphere and (b) Ellipticity. Quantities are shown in the same format as Figures 3c–3e, as a function of geocentric distance (R) and an absolute value of magnetic latitude ($|\lambda|$). The wave source region inferred by Vines et al. (2019) is shown by the gray-shaded region.

LHP was dominant in proximity to the source area only, specifically the Shabansky orbit, with a broad span in magnetic latitude and radial distance.

Then, we consider three virtual satellites that pass at different magnetic latitudes. The trajectories of the satellites are shown as dashed lines in Figures 3a and 3b, with each satellite intersecting the source region at $L = 9.7$, 8.5, and 8.0, respectively. Figures 3c–3e show the Poynting flux and wave ellipticity recorded by the virtual satellites. In Figure 3c, at the highest magnetic latitude, when the satellite's position exceeds the wave source's latitude at $R \leq 8.7 R_E$, the Poynting flux is positive $(S_{||} > 0)$, signifying wave propagation parallel to the magnetic field away from the magnetic equator, or toward the northern ionosphere. Within the source region that spans $8.7 \leq R \leq 9.2$ R_E, indicated by the gray area in Figure 3c, the satellite detects wave activity with no dominant direction in the Poynting flux. Beyond $R > 9.2 R_E$, the satellite is positioned at magnetic latitudes lower than the source, resulting in a negative Poynting flux $(S_{||} < 0)$, which indicates wave propagation in the antiparallel direction toward the southern hemisphere. When the satellite is located far from the source within the inner L-shells, it exhibits linear polarization. As it transitions to the outer L-shells, the polarization gradually shifts from linear to left-handed polarization.

In the case of the second satellite shown in Figure 3d, the Poynting flux is more clearly illustrated across different magnetic latitudes, with its direction reversed and the wave source located between. Thus, $S_{||} > 0$ for $R \leq 8.21$ R_E, $S_{||} \sim 0$ for $8.21 \leq R \leq 8.6$ R_E, and $S_{||} < 0$ for $R \geq 8.6$ R_E. Here, the satellite is near the source region within the inner L-shells; the waves are LHP and change to linear polarization when it moves toward the outer L-shells. Similarly, as the satellite traverses the magnetic equator in Figure 3e, the waves exhibit LHP for the inner L-shells near the source region (indicated by the gray shaded area in Figure 3e) without prevailing Poynting flux, signifying bidirectional Poynting flux. For the outer L-shells, the virtual satellite also detects antiparallel propagating EMIC waves directed toward the south pole, consistent with the source locations at higher magnetic latitudes in the northern hemisphere.

To compare the simulations with observations, we further examine the EMIC wave event captured by the MMS satellites on 2015-10-28 from 14:30-17:15 UT, as described in Vines et al. (2019). Here, the Poynting flux and ellipticity of the wave train are shown in Figure 4 in the same format as the virtual satellite paths in Figures 3c–3e. Each point shown in Figure 4 is derived from the average of the Poynting flux ($S_{||}$ and S_{tot}) and ellipticities at that time over the frequencies of $0.33 f_{ci}$ to $0.66 f_{ci}$. This frequency range captures the peak emission of the proton-band

EMIC wave while reducing the contribution of non-associated broadband emission. $S_{\max}$ is then the maximum of the averaged S_{tot} over the full interval. Because MMS2 measurements were taken in the southern hemisphere, and the wave source region was also inferred to be in the southern hemisphere, the observations in Figure 4 have been "mirrored" to the northern hemisphere. Values of $S_{\|}$ are multiplied by -1 (since in the south, parallel Poynting flux indicates equatorward propagation), and the absolute value of the magnetic latitudes is shown (see also Figure 1 of Vines et al. (2019)). The field-aligned Poynting flux shifts from positive to negative values as MMS2 passes above, through, and then below the source region. The polarization is linear to LHP around $9.5R_E$, then becomes more LHP, though the trend is not quite as clear when MMS is at larger radial distances. In general, this result is very consistent with the simulations, particularly with the virtual satellite path 2 in Figure 3.

3. Discussion and Summary

Although the generation of EMIC waves via ions undergoing Shabansky orbits has been explored (e.g., McCollough et al., 2012; Shabansky, 1971), clear evidence that the source of the waves is located at different magnetic latitudes for different L-shells in a compressed magnetic field configuration has only recently been observed (e.g., Noh et al., 2023; Vines et al., 2019). In this paper, we provide solid evidence of the previous theory and observations about the location of the EMIC wave generation in the outer magnetosphere. Our findings are consistent with observations, showing that if the satellite's position is below the source's magnetic latitude in the same hemisphere, we predict that the Poynting flux will flow toward the equator. Conversely, a poleward Poynting flux is detected when the satellite is above the source's magnetic latitude.

We show that waves exhibit linear polarization even at the magnetic equator in the outer magnetosphere, while LHP is mostly confined to regions near the source. Previous statistical analysis using the Cluster spacecraft indicated that LHP prevails in the outer magnetosphere ($r \geq 7$ $\mathrm{R_E}$), whereas linear polarization is more dominant closer to Earth (Allen et al., 2015). Our simulation is consistent with the statistical pattern in the noon sector and provides theoretical insight into the polarization patterns seen in the outer magnetosphere. However, the polarization state can also be influenced by factors such as heavier ion concentration and wave frequency, which should be considered in the future.

The simulations examine the interhemispheric propagation of EMIC waves when a single source is located off-equator in the northern hemisphere. In the hemisphere closer to the source, the wave exhibits minimal spreading, enabling it to concentrate on a single field line and reach the ionosphere with significant amplitude. In contrast, in the opposite hemisphere, waves do not penetrate effectively because wave power disperses across field lines to different L-shells along an extended ray path. This phenomenon results in a hemispherically asymmetric occurrence of EMIC waves at higher magnetic latitudes.

Ground-based magnetometer observations indicated an asymmetry in wave occurrences between the southern and northern hemispheres, with a higher incidence detected during local summer (Regi et al., 2017). During the summer, the geographic equatorial plane is positioned at higher magnetic latitudes due to Earth's magnetic field tilt, which may cause a difference in growth rates between the north and south. Thus, it is possible to have an asymmetric occurrence rate at the ground. E.-H. Kim and Johnson (2023) numerically explored the impact of dipole tilt on the generation and propagation of EMIC waves. They revealed that the waves could reach the ground strongly during the local summer. Still consistent with the observations by Regi et al. (2017), our results here suggest an additional scenario that can lead to interhemispheric asymmetries in wave power and characteristics observed by ground magnetometers. With a source region at a higher magnetic latitude in one hemisphere due to the interhemispherically asymmetric structure of the magnetic field with non-zero dipole tilt, the EMIC growth rate, in general, will exhibit an interhemispheric asymmetry. For observations of large L-shells, this asymmetry could be further impacted by whether that source location occurs in the hemisphere during local summer versus local winter.

While LHP EMIC waves propagate toward Earth, the wave polarization changes from LHP to linear polarization, as predicted by previous simulations (Hu & Denton, 2009; E.-H. Kim & Johnson, 2016; Denton, 2018). When waves approach Earth, the ratio between the wave frequency and the local ion cyclotron frequency (ω/ω_{ci}) becomes of the order of $10^{-2} - 10^{-3}$ near $R \sim 1 - 3(\mathrm{R}_E)$ for the given condition. In the dispersion relation, the LHP EMIC waves can be coupled with the shear Alfvén wave branches for $\omega \ll \omega_{ci}$. Our simulation shows the linear polarization enhanced in E_η (and B_ϕ, not shown here), which represents the shear Alfvén waves.

EMIC waves detected in the ionosphere or by ground magnetometers have shown various polarizations, including RHP, LHP, and linear polarization. At ionospheric altitudes, it has been observed that the wave signal is highly polarized within the plane perpendicular to the main magnetic field (Park et al., 2013) and the ellipticity of the waves is generally linear (H. Kim et al., 2010; Park et al., 2013), which is consistent with our simulations. However, the polarization of waves detected on the ground can be altered due to the ducting effect between the ground and the ionosphere (H. Kim et al., 2010, 2011; Mann et al., 2014). Despite the consistency between the simulations and the waves detected at the ionosphere, it is important to consider realistic ionospheric densities and ducting processes to accurately discuss the polarization of EMIC waves in the ionosphere and ground stations in the future.

We are focusing on the effect of magnetic field geometry while ignoring heavy-ion effects. Heavy ions, such as O^+, can be abundant in the outer magnetosphere and near the magnetopause (e.g., Bouhram et al., 2005; Fuselier et al., 2019; S. H. Lee et al., 2016; Zeng et al., 2020). When heavy ions are included, along with impacting growth rates and wave polarization (e.g., J. H. Lee, Blum, & Chen, 2021; J. H. Lee et al., 2019), additional cutoffs and resonances are introduced, which, in turn, prevent the propagation of EMIC waves to the ground (Denton et al., 2010; Denton, 2018; Hanzelka et al., 2023; Hu & Denton, 2009; Johnson et al., 1989, 1995; Johnson & Cheng, 1999; E.-H. Kim & Johnson, 2016). Furthermore, we consider the spatial structuring of magnetospheric plasma properties between the two hemispheres. The configuration of the magnetic field and plasma densities and composition near the magnetopause can significantly change depending on the strength and direction of the interplanetary magnetic field (IMF). The coupling of the solar wind and IMF to the magnetosphere can exhibit interhemispheric asymmetries through more enhanced ion outflow at high latitudes in one hemisphere versus the other depending on season and IMF direction (e.g., Barakat et al., 2015; Cully et al., 2003; Nowrouzi & Walsh, 2024; Yau et al., 1985). As EMIC waves travel along the field line, the wave propagation path would be influenced by this north-south asymmetry in the local plasma properties and magnetic field configurations as discussed by Noh et al. (2023). Additionally, while the propagation of ultralow frequency waves to the ground can be significantly influenced by ionospheric conductivity (e.g., Lysak et al., 2020), we do not incorporate a realistic ionosphere. Therefore, the heavy-ion effect and the more realistic magnetosphere and ionosphere configurations should be considered and remain a future work.

In summary, we demonstrate EMIC wave propagation in a non-dipole magnetic field topology in the outer magnetosphere using the Petra-M simulation code. In this case, we launched the waves off-equator in the northern hemisphere, where particles can undergo Shabansky orbits around local minima in the compressed magnetic field. Our research shows that the direction of the Poynting vector of EMIC waves consistently changes based on the local source location of the wave, which is consistent with previous observations. Additionally, EMIC waves generated off-equator can propagate along the magnetic field line and reach the ionosphere in both the northern and southern hemispheres. However, EMIC wave power at ionospheric altitudes shows significant hemispheric differences, demonstrating the contribution of off-equator source regions in the outer dayside magnetosphere to interhemispheric asymmetries in ionospheric and ground observations.

Data Availability Statement

The full-wave simulation data are available in E.-H. Kim, Shiraiwa, et al. (2024). MMS data used in this article are publicly available at the MMS Science Data Center (https://lasp.colorado.edu/mms/sdc/public/). MMS data shown here are directly derived from that used and described in Vines et al. (2019).

Acknowledgments
The authors acknowledge support from the National Science Foundation Grants AGS-2131013, AGS-2247395, AGS-2133837, AGS-2247398, AGS-2247396, and AGS-2013648, the National Aeronautics and Space Administration (NASA) Grant 80NSSC20K0704, 80NSSC22K0515, 80NSSC23K0899, 80NSSC21K0132 and 80NSSC19K0270, the National Research Foundation of Korea Grant NRF-2023R1A2C1002994, the Magnetospheric Multiscale mission under NASA contract NNG04EB99C, the Department of Energy contract number DE-AC02-09CH11466, DE-SC0024369, DE-AC02-05CH11231, and NERSC award FES-ERCAP0027700.

References

Albert, J. M., & Bortnik, J. (2009). Nonlinear interaction of radiation belt electrons with electromagnetic ion cyclotron waves. *Geophysical Research Letters*, *36*(12), L12110. https://doi.org/10.1029/2009GL038904

Allen, R. C., Zhang, J. C., Kistler, L. M., Spence, H. E., Lin, R. L., Dunlop, M. W., & Andre, M. (2013). Multiple bidirectional EMIC waves observed by Cluster at middle magnetic latitudes in the dayside magnetosphere. *Journal of Geophysical Research*, *118*(10), 6266–6278. https://doi.org/10.1002/jgra.50600

Allen, R. C., Zhang, J.-C., Kistler, L. M., Spence, H. E., Lin, R.-L., Klecker, B., et al. (2015). A statistical study of EMIC waves observed by cluster: 1. Wave properties. *Journal of Geophysical Research: Space Physics*, *120*(7), 5574–5592. https://doi.org/10.1002/2015JA021333

Allen, R. C., Zhang, J.-C., Kistler, L. M., Spence, H. E., Lin, R.-L., Klecker, B., et al. (2016). A statistical study of EMIC waves observed by cluster: 2. Associated plasma conditions. *Journal of Geophysical Research: Space Physics*, *121*(7), 6458–6479. https://doi.org/10.1002/2016JA022541

Anderson, B. J., Erlandson, R. E., Engebretson, M. J., Alford, J., & Arnoldy, R. L. (1996). Source region of 0.2 to 1.0 Hz geomagnetic pulsation bursts. *Geophysical Research Letters*, *23*(7), 769–772. https://doi.org/10.1029/96GL00659

Barakat, A. R., Eccles, J. V., & Schunk, R. W. (2015). Effects of geographic-geomagnetic pole offset on ionospheric outflow: Can the ionosphere wag the magnetospheric tail? *Geophysical Research Letters*, *42*(20), 8288–8293. https://doi.org/10.1002/2015GL065736

Bashir, M. F., & Ilie, R. (2021). The first observation of N+ electromagnetic ion cyclotron waves. *Journal of Geophysical Research: Space Physics*, *126*(3), e2020JA028716. https://doi.org/10.1029/2020JA028716

Bertelli, N., Shiraiwa, S., Helou, W., Milanesio, D., & Tierens, W. (2023). Benchmark between antenna code TOPICA, RAPLICASOL and Petra-M for the ICRH ITER antenna. *AIP Conference Proceedings*, *2984*(1), 060006. https://doi.org/10.1063/5.0162415

Bertelli, N., Shiraiwa, S., & Ono, M. (2022). 3D full wave fast wave modeling with realistic HHFW antenna geometry and SOL plasma in NSTX-U. *Nuclear Fusion*, *62*(12), 126046. https://doi.org/10.1088/1741-4326/ac9690

Blum, L. W., Remya, B., Denton, M. H., & Schiller, Q. (2020). Persistent EMIC wave activity across the nightside inner magnetosphere. *Geophysical Research Letters*, *47*(6), e2020GL087009. https://doi.org/10.1029/2020GL087009

Bouhram, M., Klecker, B., Paschmann, G., Haaland, S., Hasegawa, H., Blagau, A., et al. (2005). Survey of energetic O+ ions near the dayside mid-latitude magnetopause with Cluster. *Annales Geophysicae*, *23*(4), 1281–1294. https://doi.org/10.5194/angeo-23-1281-2005

Chen, H., Gao, X., Lu, Q., & Wang, S. (2019). Analyzing EMIC waves in the inner magnetosphere using long-term van allen probes observations. *Journal of Geophysical Research: Space Physics*, *124*(9), 7402–7412. https://doi.org/10.1029/2019JA026965

Cheng, C. Z. (1995). Three-dimensional magnetospheric equilibrium with isotropic pressure. *Geophysical Research Letters*, *22*(17), 2401–2404. https://doi.org/10.1029/95GL02308

Cornwall, J. M. (1965). Cyclotron instabilities and electromagnetic emission in the ultra low frequency and very low frequency ranges. *Journal of Geophysical Research*, *70*(1), 61–69. https://doi.org/10.1029/JZ070i001p00061

Cully, C. M., Donovan, E. F., Yau, A. W., & Arkos, G. G. (2003). Akebono/suprathermal mass spectrometer observations of low-energy ion outflow: Dependence on magnetic activity and solar wind conditions. *Journal of Geophysical Research*, *108*(A2). https://doi.org/10.1029/2001JA009200

Denton, R. E. (2018). Electromagnetic ion cyclotron wavefields in a realistic dipole field. *Journal of Geophysical Research: Space Physics*, *123*(2), 1208–1223. https://doi.org/10.1002/2017JA024886

Denton, R. E., Engebretson, M. J., Keiling, A., Walsh, A. P., Gary, S. P., Décréau, P. M. E., et al. (2010). Multiple harmonic ULF waves in the plasma sheet boundary layer: Instability analysis. *Journal of Geophysical Research*, *115*(A12), A12224. https://doi.org/10.1029/2010JA015928

Denton, R. E., Takahashi, K., Galkin, I. A., Nsumei, P. A., Huang, X., Reinisch, B. W., et al. (2006). Distribution of density along magnetospheric field lines. *Journal of Geophysical Research*, *111*(A10), 04213. https://doi.org/10.1029/2005JA011414

Engebretson, M. J., Posch, J. L., Capman, N. S. S., Campuzano, N. G., Bělik, P., Allen, R. C., et al. (2018). MMS, Van Allen probes, GOES 13, and ground-based magnetometer observations of EMIC wave events before, during, and after a modest interplanetary shock. *Journal of Geophysical Research: Space Physics*, *123*(10), 8331–8357. https://doi.org/10.1029/2018JA025984

Fuselier, S. A., Mukherjee, J., Denton, M. H., Petrinec, S. M., Trattner, K. J., Toledo-Redondo, S., et al. (2019). High-density O+ in Earth's outer magnetosphere and its effect on dayside magnetopause magnetic reconnection. *Journal of Geophysical Research: Space Physics*, *124*(12), 10257–10269. https://doi.org/10.1029/2019JA027396

Hanzelka, M., Li, W., Ma, Q., Qin, M., Shen, X.-C., Capannolo, L., & Gan, L. (2023). Full-wave modeling of EMIC wave packets: Ducted propagation and reflected waves. *Frontiers in Astronomy and Space Sciences*, *10*. https://doi.org/10.3389/fspas.2023.1251563

Hu, Y., & Denton, R. E. (2009). Two-dimensional hybrid code simulation of electromagnetic ion cyclotron waves in a dipole magnetic field. *Journal of Geophysical Research*, *114*(A12), A12217. https://doi.org/10.1029/2009JA014570

Johnson, J. R., Chang, T., & Crew, G. B. (1995). A study of mode conversion in an oxygen-hydrogen plasma. *Physics of Plasmas*, *2*(4), 1274–1284. https://doi.org/10.1063/1.871339

Johnson, J. R., Chang, T., Crew, G. B., & Andre, M. (1989). Equatorially generated ULF waves as a source for the turbulence associated with ion conics. *Geophysical Research Letters*, *16*(12), 1469–1472. https://doi.org/10.1029/GL016i012p01469

Johnson, J. R., & Cheng, C. Z. (1999). Can ion cyclotron waves propagate to the ground? *Geophysical Research Letters*, *26*(6), 671–674. https://doi.org/10.1029/1999gl900074

Jordanova, V. K., Farrugia, C. J., Thorne, R. M., Khazanov, G. V., Reeves, G. D., & Thomsen, M. F. (2001). Modeling ring current proton precipitation by electromagnetic ion cyclotron waves during the May 14-16, 1997, storm. *Journal of Geophysical Research*, *106*(A1), 7–22. https://doi.org/10.1029/2000JA002008

Jun, C.-W., Miyoshi, Y., Kurita, S., Yue, C., Bortnik, J., Lyons, L., et al. (2021). The characteristics of EMIC waves in the magnetosphere based on the Van Allen Probes and Arase observations. *Journal of Geophysical Research: Space Physics*, *126*(6), e2020JA029001. https://doi.org/10.1029/2020JA029001

Kim, E.-H., & Johnson, J. R. (2016). Full-wave modeling of EMIC waves near the He^+ gyrofrequency. *Geophysical Research Letters*, *43*(1), 13–21. https://doi.org/10.1002/2015GL066978

Kim, E.-H., & Johnson, J. R. (2023). Magnetic tilt effect on externally driven electromagnetic ion cyclotron (EMIC) waves. *Geophysical Research Letters*, *50*(6), e2022GL101544. https://doi.org/10.1029/2022GL101544

Kim, E.-H., Johnson, J. R., Kim, H., & Lee, D.-H. (2015). Inferring magnetospheric heavy ion density using EMIC waves. *Journal of Geophysical Research: Space Physics*, *120*(8), 6464–6473. https://doi.org/10.1002/2015JA021092

Kim, E.-H., Ono, M., Shiraiwa, S., Bertelli, N., Poulos, M., Van Compernolle, B., et al. (2024). Full-wave simulations on helicon and parasitic excitation of slow waves near the edge plasma. *Physics of Plasmas*, *31*(10), 102102. https://doi.org/10.1063/5.0222413

Kim, E.-H., Shiraiwa, S., Bertelli, N., Cheng, C. Z., Ono, M., Park, K., & Johnson, J. R. (2023). Applications of the Petra-M simulation code for the magnetospheric Physics. *AIP Conference Proceedings*, *2984*, 130001. https://doi.org/10.1063/5.0164070

Kim, E.-H., Shiraiwa, S., Johnson, J. R., Bertelli, N., Vines, S., Kim, K.-H., et al. (2024). Propagation of EMIC waves from Shabansky orbits in the dayside magnetosphere [dataset]. *Princeton Plasma Physics Laboratory, Princeton University*. https://doi.org/10.34770/e3m1-rs25

Kim, G.-J., Kim, K.-H., Lee, D.-H., Kwon, H.-J., & Park, J.-S. (2016). Occurrence of EMIC waves and plasmaspheric plasmas derived from THEMIS observations in the outer magnetosphere: Revisit. *Journal of Geophysical Research (Space Physics)*, *121*(10), 9443–9458. https://doi.org/10.1002/2016JA023108

Kim, H., Lessard, M. R., Engebretson, M. J., & Luhr, H. (2010). Ducting characteristics of Pc 1 waves at high latitudes on the ground and in space. *Journal of Geophysical Research*, *115*(A9), A09310. https://doi.org/10.1029/2010JA015323

Kim, H., Lessard, M. R., Engebretson, M. J., & Young, M. A. (2011). Statistical study of Pc1–2 wave propagation characteristics in the high-latitude ionospheric waveguide. *Journal of Geophysical Research*, *116*(A7). https://doi.org/10.1029/2010JA016355

Kim, K.-H., Jun, C.-W., Kwon, J.-W., Lee, J., Shiokawa, K., Miyoshi, Y., et al. (2024). Observation and numerical simulation of cold ions energized by EMIC waves. *Journal of Geophysical Research: Space Physics*, *129*(5), e2023JA032361. https://doi.org/10.1029/2023JA032361

Kim, K.-H., Omura, Y., Jin, H., & Hwang, J. (2017). A case study of EMIC waves associated with sudden geosynchronous magnetic field changes. *Journal of Geophysical Research: Space Physics*, *122*(3), 3322–3341. https://doi.org/10.1002/2016JA023391

Kim, M. J., Goldstein, J., Fuselier, S. A., Vines, S. K., Usanova, M. E., Gonzalez, C. A., et al. (2023). MMS observations of warm-ion (E \lessbin 100 eV) heating inside plasmaspheric plumes. *Journal of Geophysical Research: Space Physics*, *128*(11), e2023JA031771. https://doi.org/10.1029/2023JA031771

Klimushkin, D. Y., Mager, P. N., & Marilovtseva, O. S. (2010). Parallel structure of Pc1 ULF oscillations in multi-ion magnetospheric plasma at finite ion gyrofrequency. *Journal of Atmospheric and Solar-Terrestrial Physics*, *72*(18), 1327–1332. https://doi.org/10.1016/j.jastp.2010.09.019

Kozyra, J. U., Jordanova, V. K., Home, R. B., & Thorne, R. M. (1997). Modeling of the contribution of electromagnetic ion cyclotron (EMIC) waves to stormtime ring current erosion. *Geophysical Monograph Series*, *98*, 187–202. https://doi.org/10.1029/GM098p0187

Kwon, J.-W., Kim, K.-H., Jin, H., Min, K., Lee, S.-Y., & Lee, E. (2023). Energization of cold protons and helium ions by EMIC waves in the inner magnetosphere: Hybrid simulations. *Journal of Geophysical Research: Space Physics*, *128*(5), e2022JA031240. https://doi.org/10.1029/2022JA031240

Lee, D.-H., Johnson, J. R., Kim, K., & Kim, K.-S. (2008). Effects of heavy ions on ULF wave resonances near the equatorial region. *Journal of Geophysical Research*, *113*(A11), A11212. https://doi.org/10.1029/2008JA013088

Lee, J., Kim, K.-H., & Lee, E. (2021). A statistical study of low-energy ion flux enhancements by EMIC waves in the inner magnetosphere. *Journal of Geophysical Research (Space Physics)*, *126*(8), e29793. https://doi.org/10.1029/2021JA029793

Lee, J. H., Blum, L. W., & Chen, L. (2021). On the impacts of ions of ionospheric origin and their composition on magnetospheric EMIC waves. *Frontiers in Astronomy and Space Sciences*, *8*, 122. https://doi.org/10.3389/fspas.2021.719715

Lee, J. H., Turner, D. L., Toledo-Redondo, S., Vines, S. K., Allen, R. C., Fuselier, S. A., et al. (2019). MMS measurements and modeling of peculiar electromagnetic ion cyclotron waves. *Geophysical Research Letters*, *46*(21), 11622–11631. https://doi.org/10.1029/2019GL085182

Lee, S. H., Zhang, H., Zong, Q.-G., Otto, A., Rème, H., & Liebert, E. (2016). A statistical study of plasmaspheric plumes and ionospheric outflows observed at the dayside magnetopause. *Journal of Geophysical Research: Space Physics*, *121*(1), 492–506. https://doi.org/10.1002/2015JA021540

Lysak, R. L., Song, Y., Waters, C. L., Sciffer, M. D., & Obana, Y. (2020). Numerical investigations of interhemispheric asymmetry due to ionospheric conductance. *Journal of Geophysical Research: Space Physics*, *125*(7), e2020JA027866. https://doi.org/10.1029/2020JA027866

Mann, I. R., Usanova, M. E., Murphy, K., Robertson, M. T., Milling, D. K., Kale, A., et al. (2014). Spatial localization and ducting of EMIC waves: Van Allen Probes and ground-based observations. *Geophysical Research Letters*, *41*(3), 785–792. https://doi.org/10.1002/2013GL058581

Mauk, B. H. (1982). Helium resonance and dispersion effects on geostationary Alfven/ion cyclotron waves. *Journal of Geophysical Research*, *87*(A11), 9107–9119. https://doi.org/10.1029/JA087iA11p09107

McCollough, J. P., Elkington, S. R., & Baker, D. N. (2012). The role of Shabansky orbits in compression-related electromagnetic ion cyclotron wave growth. *Journal of Geophysical Research*, *117*(A1), A01208. https://doi.org/10.1029/2011JA016948

McCollough, J. P., Elkington, S. R., Usanova, M. E., Mann, I. R., Baker, D. N., & Kale, Z. C. (2010). Physical mechanisms of compressional EMIC wave growth. *Journal of Geophysical Research*, *115*(A10), A10214. https://doi.org/10.1029/2010JA015393

Mikhailova, O. S., Mager, P. N., & Klimushkin, D. Y. (2019). Two modes of ion-ion hybrid waves in magnetospheric plasma. *Plasma Physics and Controlled Fusion*, *62*(2), 025026. https://doi.org/10.1088/1361-6587/ab5b32

Min, K., Lee, J., Keika, K., & Li, W. (2012). Global distribution of EMIC waves derived from THEMIS observations. *Journal of Geophysical Research*, *117*(A5), A05219. https://doi.org/10.1029/2012JA017515

Mohebujjaman, M., Shiraiwa, S., Labombard, B., Wright, J. C., & Uppalapati, K. K. (2023). Scalability analysis of direct and iterative solvers used to model charging of superconducting pancake solenoids. *Engineering Research Express*, *5*(1), 015045. https://doi.org/10.1088/2631-8695/acbd85

Mouikis, C. G., Kistler, L. M., Baumjohann, W., Lund, E. J., Korth, A., Klecker, B., et al. (2002). Equator-S observations of He+ energization by EMIC waves in the dawnside equatorial magnetosphere. *Geophysical Research Letters*, *29*(10), 7–74. https://doi.org/10.1029/2001GL013899

Noh, S.-J., Kim, H., Lessard, M., Engebretson, M., Pilipenko, V., Kim, E.-H., et al. (2022). Statistical study of EMIC wave propagation using space-ground conjugate observations. *Journal of Geophysical Research: Space Physics*, *127*(7), e2022JA030262. https://doi.org/10.1029/2022JA030262

Noh, S.-J., Kim, H., Ozturk, D., Kuzichev, I., Xu, Z., Zhang, H., et al. (2023). Interhemispheric observations of ULF waves caused by foreshock transients under quiet solar wind conditions. *Journal of Geophysical Research: Space Physics*, *128*(9), e2023JA031596. https://doi.org/10.1029/2023JA031596

Nowrouzi, N., & Walsh, B. M. (2024). Interhemispheric asymmetry in the seasonal ionospheric outflow. *Geophysical Research Letters*, *51*(14), e2024GL108556. https://doi.org/10.1029/2024GL108556

Omidi, N., Thorne, R. M., & Bortnik, J. (2011). Hybrid simulations of EMIC waves in dipolar magnetic field. *Journal of Geophysical Research*, *116*(A9), A09231. https://doi.org/10.1029/2011JA016511

Pakhotin, I. P., Mann, I. R., Sydorenko, D., & Rankin, R. (2022). Novel EMIC wave propagation pathway through buchsbaum resonance and inter-hemispheric wave interference: Swarm observations and modeling. *Geophysical Research Letters*, *49*(10), e2022GL098249. https://doi.org/10.1029/2022GL098249

Park, J., Luhr, H., & Rauberg, J. (2013). Global characteristics of Pc1 magnetic pulsations during solar cycle. *Annales Geophysicae*, *31*(9), 1507–1520. https://doi.org/10.5194/angeo-31-1507-2013

Regi, M., Marzocchetti, M., Francia, P., & De Lauretis, M. (2017). A statistical analysis of Pc1-2 waves at a near-cusp station in Antarctica. *Earth Planets and Space*, *69*(1), 152. https://doi.org/10.1186/s40623-017-0738-8

Roux, A., Perraut, S., Rauch, J. L., de Villedary, C., Kremser, G., Korth, A., & Young, D. T. (1982). Wave-particle interactions near Ω_{He+} observed on board GEOS 1 and 2: 2. Generation of ion cyclotron waves and heating of He+ ions. *Journal of Geophysical Research*, *87*(A10), 8174–8190. https://doi.org/10.1029/JA087iA10p08174

Saikin, A. A., Zhang, J.-C., Allen, R. C., Smith, C. W., Kistler, L. M., Spence, H. E., et al. (2015). The occurrence and wave properties of H+-, He+-and O+-band EMIC waves observed by the Van Allen Probes. *Journal of Geophysical Research: Space Physics*, *120*(9), 7477–7492. https://doi.org/10.1002/2015JA021358

Shabansky, V. P. (1971). Some processes in the magnetosphere. *Space Science Reviews*, *12*(3), 299–418. https://doi.org/10.1007/BF00165511

Shiraiwa, S., Bertelli, N., Bilato, R., Bonoli, P., Helou, W., Hillairet, J., et al. (2023a). Verification/validation and physics model extension in high fidelity 3D RF full wave simulations on Petra-M. *AIP Conference Proceedings*, *2984*(1), 030007. https://doi.org/10.1063/5.0163275

Shiraiwa, S., Bertelli, N., Tierens, W., Bilato, R., Hillairet, J., Myra, J., et al. (2023). Magnetic potential based formulation for linear and non-linear 3D RF sheath simulation. *Nuclear Fusion*, *63*(2), 026024. https://doi.org/10.1088/1741-4326/aca6f9

Shiraiwa, S., Fredian, T., Hillairet, J., & Stillerman, J. (2016). \piScope: Python based scientific workbench with MDSplus data visualization tool. *Fusion Engineering and Design*, *112*, 835–838. https://doi.org/10.1016/j.fusengdes.2016.06.050

Shiraiwa, S., Wright, J. C., Bonoli, P. T., Kolev, T., & Stowell, M. (2017). RF wave simulation for cold edge plasmas using the MFEM library. *EPJ Web of Conferences*, *157*, 03048. https://doi.org/10.1051/epjconf/201715703048

Shprits, Y. Y., Drozdov, A. Y., Spasojevic, M., Kellerman, A. C., Usanova, M. E., Engebretson, M. J., et al. (2016). Wave-induced loss of ultra-relativistic electrons in the Van Allen radiation belts. *Nature Communications*, *7*(1), 12883. https://doi.org/10.1038/ncomms12883

Stern, D. P. (1967). Geomagnetic euler potentials. *Journal of Geophysical Research*, *72*(15), 3995–4005. https://doi.org/10.1029/JZ072i015p03995

Summers, D., & Thorne, R. M. (2003). Relativistic electron pitch-angle scattering by electromagnetic ion cyclotron waves during geomagnetic storms. *Journal of Geophysical Research*, *108*(A4), 1143. https://doi.org/10.1029/2002JA009489

Taylor, W. W. L., & Lyons, L. R. (1976). Simultaneous equatorial observations of 1- to 30-Hz waves and pitch angle distributions of ring current ions. *Journal of Geophysical Research*, *81*(34), 6177–6183. https://doi.org/10.1029/JA081i034p06177

Thorne, R. M., Horne, R. B., Jordanova, V. K., Bortnik, J., & Glauert, S. (2006). Interaction of EMIC waves with thermal plasma and radiation belt particles. *Geophysical Monograph Series*, *169*, 213–223. https://doi.org/10.1029/169GM14

Toledo-Redondo, S., Lee, J. H., Vines, S. K., Albert, I. F., André, M., Castilla, A., et al. (2024). Statistical observations of proton-band electromagnetic ion cyclotron waves in the outer magnetosphere: Full wavevector determination. *Journal of Geophysical Research: Space Physics*, *129*(5), e2024JA032516. https://doi.org/10.1029/2024JA032516

Usanova, M. E. (2021). Energy exchange between electromagnetic ion cyclotron (EMIC) waves and thermal plasma: From theory to observations. *Frontiers in Astronomy and Space Sciences*, *8*, 150. https://doi.org/10.3389/fspas.2021.744344

Usanova, M. E., Drozdov, A., Orlova, K., Mann, I. R., Shprits, Y., Robertson, M. T., et al. (2014). Effect of EMIC waves on relativistic and ultrarelativistic electron populations: Ground-based and Van Allen Probes observations. *Geophysical Research Letters*, *41*(5), 1375–1381. https://doi.org/10.1002/2013GL059024

Usanova, M. E., Mann, I. R., & Darrouzet, F. (2016). EMIC waves in the inner magnetosphere. *Geophysical Monograph Series*, *216*, 65–78. https://doi.org/10.1002/9781119055006.ch5

Vines, S. K., Allen, R. C., Anderson, B. J., Engebretson, M. J., Fuselier, S. A., Russell, C. T., et al. (2019). EMIC waves in the outer magnetosphere: Observations of an off-equator source region. *Geophysical Research Letters*, *46*(11), 5707–5716. https://doi.org/10.1029/2019GL082152

Wang, X. Y., Huang, S. Y., Allen, R. C., Fu, H. S., Deng, X. H., Zhou, M., et al. (2017). The occurrence and wave properties of EMIC waves observed by the Magnetospheric Multiscale (MMS) mission. *Journal of Geophysical Research: Space Physics*, *122*(8), 8228–8240. https://doi.org/10.1002/2017JA024237

Xu, X., & Zhou, C. (2023). Effects of cold plasma on the mode conversion from fast magnetosonic wave to electromagnetic ion cyclotron wave in the inner plasmasphere. *Journal of Geophysical Research: Space Physics*, *128*(9), e2022JA031273. https://doi.org/10.1029/2022JA031273

Xu, X., Zhou, C., Chen, L., & Horne, R. B. (2023). Modeling the propagation of fast magnetosonic waves and their conversion to electromagnetic ion cyclotron waves at low L shells. *Journal of Geophysical Research: Space Physics*, *128*(9), e2022JA031271. https://doi.org/10.1029/2022JA031271

Yao, Z., Dunn, W. R., Woodfield, E. E., Clark, G., Mauk, B. H., Ebert, R. W., et al. (2021). Revealing the source of Jupiter's x-ray auroral flares. *Science Advances*, *7*(28), eabf0851. https://doi.org/10.1126/sciadv.abf0851

Yau, A. W., Lenchyshyn, L., Shelley, E. G., & Peterson, W. K. (1985). Energetic auroral and polar ion outflow at DE 1 altitudes Magnitude, composition, magnetic activity dependence, and long-term variations. *Journal of Geophysical Research*, *90*(A9), 8417–8432. https://doi.org/10.1029/ja090ia09p08417

Yu, J., Li, L. Y., Cui, J., Cao, J. B., & Wang, J. (2019). Effect of hot He+ ions on the electron pitch angle scattering driven by H+, He+, and O+ band EMIC waves. *Geophysical Research Letters*, *46*(12), 6306–6314. https://doi.org/10.1029/2019GL083456

Yuan, Z., Zhao, Y., Yu, X., Xue, Z., & Deng, D. (2024). Duct effect of magnetic dips on the propagation of EMIC waves in Jupiter's magnetosphere with observations of Juno. *Geophysical Research Letters*, *51*(16), e2024GL109691. https://doi.org/10.1029/2024GL109691

Zeng, C., Wang, C., Duan, S., Dai, L., Fuselier, S. A., Burch, J. L., et al. (2020). Statistical study of oxygen ions abundance and spatial distribution in the dayside magnetopause boundary layer: MMS observations. *Journal of Geophysical Research: Space Physics*, *125*(7), e2019JA027323. https://doi.org/10.1029/2019JA027323